JOURNAL OF MATERIALS SCIENCE **40** (2005) 1141 – 1152

Effects of nematic polymer liquid crystal on crystallization and structure of PET/Vectra blends

G. GEORGIEV*, P. CEBE†
Department of Physics and Astronomy, Tufts University, Medford, MA 02155, USA
E-mail: peggy.cebe@tufts.edu

M. CAPEL‡
Biology Department, Brookhaven National Laboratory, Upton, NY, USA

We investigate the effects of a nematic liquid crystalline polymer, Vectra A, on the structure and properties of its blends with a semicrystalline polymer, poly(ethylene terephthalate), PET. PET/Vectra blend composition ranged from 100/0 to 60/40. Real-time, *in situ* studies of isothermal and non-isothermal melt crystallizations of these blends were conducted using simultaneous wide and small angle X-ray scattering (WAXS and SAXS), differential scanning calorimetry (DSC), and quantitative polarizing optical microscopy. All techniques confirm that the addition of Vectra nematic liquid crystal delays the onset of crystallization, and affects the degree of crystallinity and structural parameters such as Bragg long period, lamellar thickness and linear stack crystallinity. SAXS results indicate that some of the Vectra component penetrates into the interlamellar regions of the crystal stacks. Vectra interrupts the entangled polymer network making it more difficult for lamellar crystals to nucleate. Slower nucleation and growth result in increased perfection of the PET crystals grown isothermally, but reduces the crystallization temperature of PET crystals grown non-isothermally causing these crystals to be less perfect.

1. Introduction

The addition of nematic liquid crystal polymer (LCP) to a semicrystalline polymer is used to improve the melt processability of the latter through the "lubricating" effect of the liquid crystalline component. Below the temperature of the isotropic-to-nematic phase transition, the nematic liquid crystal polymer can form aligned, phase-separated regions within the highly entangled melt of the semicrystalline polymer. These nematic domains have lower overall viscosity and greatly enhance the flow properties of the melt. One important thermotropic LCP is Vectra A, comprising 27 mol% 2,6-hydroxynaphthoic acid and 73 mol% of p-hydroxybenzoic acid. Vectra A has enhanced moldability arising from its random naphthoic units that reduce the melting range while maintaining liquid crystallinity [1].

Vectra LCP has been added to a number of semicrystalline polymers including poly(etheretherketone) (PEEK) [2], polypropylene (PP) [3–5], poly(butylene terephthalate) (PBT) [6], nylon [7], and poly(ethylene terephthalate) (PET) [8–16]. For PP/Vectra blends, it was found [5] that the crystallization rate was enhanced by Vectra addition, with Vectra acting as nucleation sites for crystal growth. Similar result was found for the effect of other LCPs on crystallization of PET [17], and the suggestion was made that LCPs may enhance the crystallization rate for low LCP content, while retarding the rate for higher LCP content. In PBT/Vectra blends, the rate of crystallization was enhanced by Vectra addition, without much effect on crystallinity [6].

For PET, the addition of Vectra impacts the rheological properties and structure of samples crystallized from the melt. Perkins [16] reported that, depending upon composition, the LCP exists as dispersed globules within the PET matrix, causing poor adhesion. The morphology of injection molded samples studied by Silverstein and Hiltner [15] showed typical skin-core effect, with the degree of chain orientation decreasing from the exterior to interior of the sample. As Vectra composition increased, there was a greater degree of entanglement among LCP domains. Thermal analysis by Magagnini *et al*. [12] and Chang-Chien and Denn [14] showed that crystallization rate of PET was slowed by Vectra addition while Liang *et al*. [8] reported that Vectra enhanced crystallization from the glassy state, but retarded crystallization from the melt. Tang *et al*. [11] used NMR to show that Vectra can penetrate the PET regions upon annealing of the melt.

Present address: Physics Department, Northeastern University, Boston, MA, USA.
†Author to whom all correspondence should be addressed.
‡*Present address*: Advanced Photon Source, Argonne National Laboratory, Chicago, IL, USA.

Real-time simultaneous wide (WAXS) and small (SAXS) angle X-ray scattering studies can provide additional information about the crystallization kinetics and structure of PET/Vectra blends. Not only can the crystallinity development with time be examined, but also the impact of Vectra on formation of periodic lamellar stacks can be assessed. There are many X-ray scattering studies of homopolymer PET crystallized either from the glass [18–21] or melt states [22–29]. In the present study, we apply optical, thermal, and X-ray scattering techniques to PET/Vectra melt crystallized blends. We investigate the kinetics of crystallization and the formation and perfection of the PET lamellae. Although Vectra nematic liquid crystalline polymer is immiscible in PET, nonetheless, Vectra is not excluded from the amorphous interphase between lamellae. From analysis of the electron density correlation function and the interface distribution function, we find that Vectra increases the long period and crystalline lamellar thickness in PET/Vectra blends, compared to homopolymer PET.

The possibility of transesterification reaction cannot be absolutely avoided during melt processing, even for homopolymer PET [30]. However, the likelihood for transesterification reaction increases as melt temperature and holding time increase. Transesterification between Vectra liquid crystalline polymer and polycarbonates does not occur until 320°C [31], and the transesterification of homopolymer PET is shown to be on the minute timescale at temperatures comparable to those in our study [30]. In our study, we minimize the possibility for transesterification by preparing the films at the lowest possible temperature, and shortest processing time, with drying to less than 0.01% water content before blending.

2. Experimental section

Plaques of Vectra A liquid crystalline polymer comprising 27 mol% 2,6-hydroxynaphthoic acid (HNA) and 73 mol% of *p*-hydroxybenzoic acid [13, 14], blended with PET were provided by Dr. J.S. Chung of the former Allied Signal Corp. with different composition of PET/Vectra, viz., 100/0, 90/10, 80/20, 70/30 and 60/40 wt%. The PET was an experimental product of the former Allied Signal Corp. with intrinsic viscosity of 0.92 dl/g, measured in 60/40 phenol/trichloroethylene solution, giving a molecular weight of 25,000 g/mol calculated from the Mark-Houwink equation with $a = 0.640$ and $K = 14 \times 10^{-4}$ dl/g [30, p. V105]. The blend preparation was performed using a lab scale Haake twin screw conical extruder at 150 rpm, temperature of 290°C, with residence time of 40 s. To minimize transesterification, the lowest processing time and temperature were used, and the materials were dried to moisture content less than 0.01% prior to blending.

The thermal treatment schemes included: isothermal melt crystallization at 225°C, followed by immediate reheating; or non-isothermal crystallization by cooling at 5°C/min, to 50°C followed by reheating. For isothermal crystallization studies, the samples were initially briefly melted at 290°C, and then cooled at a rate of 5°C/min, to 225°C where they were held for 30 min. Then they were cooled either to room temperature for DSC studies, or to 215°C for X-ray and optical studies, and then reheated to 290°C. The cooling to 215°C during X-ray studies allowed the resolution of any structures resulting from the isothermal treatment while preventing additional crystallization that could occur during cooling to room temperature.

The following tests were used to examine the likelihood of transesterification reaction occurring in our PET/Vectra blends. An abusive DSC technique was performed, which subjects the blends to high temperature cyclic holding. Both the homopolymer PET and the 60/40 blend experienced a 0.3°C decrease in melting point after 20 min of abuse at 290°C. Through six cycles of holding for 10 min at 290°C (total 1 hour of holding) the melting points of homopolymer PET and the 60/40 blend decreased by 3–4°C. When the temperature of abuse was increased to 330°C, after six cycles, the homopolymer melting point decreased by 3.5°C while the 60/40 blend melting point decreased by 7.2°C. High temperatures and long holding times do cause deterioration in the thermal properties of both PET homopolymer and its blends with Vectra. However, after brief holding (2 min) at 290°C we observed no change in thermal properties (glass transition temperature, degree of crystallinity, crystallization temperature, melting temperature, or crystallization kinetics) for PET or PET/Vectra blends.

The heating and cooling for optical and X-ray studies were performed using a Mettler FP80 hot stage. For thermal analysis, a TA Instruments 2920 MDSC was used. The MDSC was calibrated using indium standard for melting point and heat flow. Sample mass was about 10–15 mg, and nitrogen purge gas was used at flow rate of 30 cc/min. To compare the crystallinities obtained with different methods, we converted the DSC mass fraction crystallinity, $f_{c,m}$, to volume fraction crystallinity, $f_{c,v}$, using:

$$f_{c,v} = (f_{c,m} \cdot \rho_a)/(\rho_c - f_{c,m}(\rho_c - \rho_a)) \qquad (1)$$

where the amorphous phase density for PET, ρ_a is 1.335 g/cc, and the crystalline unit cell density ρ_c is 1.515 g/cc [32]. Mass fraction crystallinity was found from the DSC total endotherm area using 166 J/g as the heat of fusion of 100% crystalline PET [33]. Crystallinities for isothermal and non-isothermal treatments are listed in Tables I and II, respectively.

SAXS intensity was collected using a two-dimensional, gas-filled wire detector. Wavelength was $\lambda = 0.16$ nm or 0.1366 nm, and scattering vector, q (where $q = 2\pi s = 4\pi \sin\theta/\lambda$ for θ the half-scattering angle) was calibrated using cholesterol myristate. For these isotropic samples, circular integration was used to convert the two-dimensional patterns into one-dimensional line scans. The raw intensity data are first corrected for changes in the incident beam intensity, sample absorption, and background (air, or Kapton^{TM} tape). After this level of correction, the final intensity, $I_{corr}(q)$, used for calculation of the correlation function or interface distribution function is determined (see below).

TABLE I Thermal and X-ray parameters[#] for PET/Vectra blends crystallized isothermally

PET/Vectra	100/0	90/10	80/20	70/30	60/40
$f_{c,m}$ ($\pm$ 0.01)[a]	0.31	0.31	0.33	0.33	0.30
$f_{c,v}$ ($\pm$0.01)[b]	0.28	0.28	0.30	0.30	0.27
T_g, °C ($\pm$0.5)[c]	72.7	73.1	71.9	72.2	73.1
Q_i^d	n[i]	3.1	2.9	1.4	0.7
L_B, nm ($\pm$0.2)[e]	15.1	16.1	16.9	16.0	17.2
L^{max}, nm ($\pm$0.2)[f]	14.5	15.3	16.0	15.4	15.7
d_1, nm ($\pm$0.2)[f]	4.2	4.5	4.5	4.7	4.8
$d_1/L^{max\,f}$	0.29	0.30	0.28	0.31	0.30
ϕ_1($\pm$0.01)[g]	0.32	0.31	0.31	0.33	0.32
L, nm ($\pm$0.2)[h]	12.0	13.3	13.7	13.8	13.5
(σ_L, $\pm$0.1)[h]	(4.4)	(4.7)	(4.9)	(4.5)	(4.9)
d_1, nm ($\pm$0.2)[h]	3.8	5.9	5.7	6.2	3.9
(σ_1, $\pm$0.1)[h]	(2.3)	(2.3)	(2.4)	(2.0)	(2.5)
d_2, nm ($\pm$0.2)[h]	8.2	7.4	8.0	7.6	9.5
(σ_2, $\pm$0.1)[h]	(3.8)	(4.1)	(4.3)	(4.1)	(4.2)

[#]X-ray data are reported at the end of 30 min. isothermal crystallization at 225°C.
[a]DSC mass fraction crystallinity, $f_{c,m}$ from: (total endotherm area, J/g)/(166 J/g) [33].
[b]Volume fraction crystallinity, $f_{c,v}$ from DSC endotherm area, according to Equation 1.
[c]Glass transition temperature, measured after crystallization at 225°C.
[d]Scattering invariant determined from Equation 9. SAXS intensity is not placed on an absolute basis, so the values of Q_i are relative ones.
[e]Long period, L_B, determined from SAXS, using the maximum in $I(q)q^2$ vs. q plot
[f]Determined from SAXS, using the correlation function [38] (see Fig. 7b).
[g]Fraction of phase 1, determined from SAXS, using the correlation function self-correlation triangle [38], $\phi_1 = |A|/(|A| + Q)$ (see Fig. 7b).
[h]Long period, L, phase thickness, d_i, and variance, σ_i ($i = 1, 2, L$) determined from SAXS, using Gaussian fits to the Interface Distribution Function and assuming a stacking model with infinite stacks (ISSM) [26–28].
[i]Data not available.

TABLE II Thermal and X-ray parameters[#] for PET/Vectra blends crystallized non-isothermally

PET/vectra	90/10	60/40
$f_{c,m}$ ($\pm$0.01)[a]	0.27	0.29
$f_{c,v}$ ($\pm$0.01)[b]	0.25	0.26
L_B, nm ($\pm$0.2)[c]	12.2	11.9
L^{max}, nm ($\pm$0.2)[d]	10	9.5
d_1 ($\pm$0.2)[d]	4.5	4.2
$d_1/L^{max\,d}$	0.44	0.44
ϕ_1 ($\pm$0.01)[e]	0.45	0.44

[#]X-ray data are reported at 50C, at the end of non-isothermal crystallization by cooling at 5C/min from 290°C.
[a]DSC mass fraction crystallinity, $f_{c,m}$, from: (total endotherm area, J/g) / (166 J/g) [33].
[b]Volume fraction crystallinity, $f_{c,v}$, from DSC endotherm area, according to Equation (1).
[c]Long period, L_B, determined from SAXS, using the maximum in $I(q)q^2$ vs. q.
[d]Determined from SAXS, using the correlation function [38] (see Fig. 7b).
[e]Fraction of phase 1, determined from SAXS, using the correlation function self-correlation triangle [38], $\phi_1 = |A|/(|A| + Q)$ (see Fig. 7b).

Behind the beam stop, the intensity $I_{corr}(q)$ is linearly extrapolated to zero at $q = 0$. At high scattering vector, $I_{corr}(q \rightarrow \infty)$ is corrected to account for deviations from Porod's Law behavior and for density fluctuations. The intensity observed at high q can be written as [34]:

$$I^{obs}(q \rightarrow \infty) = I^{ideal}(q)H^2(q) + I_{FL} \qquad (2)$$

where $I^{ideal} = K_p/q^4$ (K_p is Porod's Law constant); I_{FL} is a background due to short range fluctuations in the sample density [34]; and $H^2(q)$ is the Fourier transformation of the autocorrelation of the smoothing function, describing deviations from Porod's law behavior caused by finite interphase thickness [35]. We assume a sigmoidal shape for the interphase geometry so that the form of H^2 is [35]:

$$H^2(q) = \exp(E^2q^2) \qquad (3)$$

where the parameter, E, is a measure of the width of the interphase. At high q-vector, the intensity data are fitted with three adjustable parameters (K_p, I_{FL}, E) using a Nelder-Mead simplex direct search minimization routine [36].

The final corrected intensity $I_{corr}(q)$ is used to determine the normalized reciprocal-space interference function, $G_1(q)$ defined as [32]:

$$G_1(q) = K_p - q^4 I_{corr}(q) \qquad (4)$$

The lower limit of validity of Porod's Law is estimated as the value, q_{min} of scattering vector that minimizes the area of the interference function for $q < q_{min}$ (realizing that G_1 is zero for $q > q_{min}$) [34]. After this determination of q_{min}, the real-space interface distribution function, $g_1(r)$, is found by Fourier Transformation of $G_1(q)$ [34]:

$$g_1(r) = (2\pi^2)^{-1} \int G_1(q)\cos(qr)dq \qquad (5)$$

Morphological parameters are derived from the interface distribution function (IDF) using the methods described by Stribeck [25–28] and Ruland [25]. On the assumption that the variations of the interface distances follow Gaussian distributions, the IDF can be written as the sum of weighted Gaussians, h_i, with centers at r_i, through [25]:

$$g_1(r) = \Sigma w_i h_i(r - r_i) \qquad (6)$$

The sum runs from $i = 1$ to ∞, with the Gaussians weighted by the w_i. Following Stribeck's method, we use normalized Gaussians of the form [25–28]:

$$h_i = \left(2\pi\sigma_i^2\right)^{-0.5} \exp\left(-r^2/\left(2g\sigma_i^2\right)\right) \qquad (7)$$

The Nelder-Mead simplex direct search minimization strategy [36] is used to determine the fitting parameters: w_i, r_i, and standard deviations, σ_i. In practice, once i exceeded about 30 in the summation of Equation 6, there was no noticeable improvement in the Gaussian fits to the IDF.

As described by Stribeck and Ruland [25], the spacings, r_i, of the interfaces are not independent of one another; higher order interface spacings are multiples of lower order interface spacings. We report the first three spacings, d_1 and d_2 (thicknesses of phase 1 and phase 2, respectively) and $L(L = d_1 + d_2)$. Furthermore, the

weights and standard deviations are dependent upon the stack size (whether finite or infinite stack size is assumed) and statistics of lamellar stacking (whether a stacking model or lamellar model is assumed) [25]. The stacking model with infinite stack size (ISSM) produced the best fit to our data.

The normalized one-dimensional electron density correlation function, $\gamma(r)$, is evaluated from [37]:

$$\gamma(r) = \int q^2 I_{\text{corr}}(q) \cos(qr) dq \Big/ \int q^2 I_{\text{corr}}(q) dq \tag{8}$$

The parameters: invariant, Q, long period, $L^{\max}$; thickness of phase one, d_1; and χ_c, the linear crystallinity within the lamellar stacks from the self-correlation triangle, are determined according to the method of Strobl and Schneider [38]. For comparison, Bragg's long period, L_B, is deduced from the location of the peak in $I_{\text{corr}}(q)q^2$ vs. q plot.

The scattering invariant is found from [39, 40]:

$$Q = \int I_{\text{corr}}(q) q^2 dq (9) \tag{9}$$

For a two-phase system, the invariant can be written as:

$$Q = \phi_s \phi_c (1 - \phi_c)(\Delta\rho)^2 \tag{10}$$

where ϕ_c and $(1 - \phi_c)$ are, respectively, the volume fractions of the crystalline and amorphous phases, and $\Delta\rho = \rho_c - \rho_a$ is the density difference converted to electrons per unit volume. ϕ_s is the spherulite fill fraction.

Wide angle X-ray scattering intensity was collected simultaneously with the SAXS intensity using a Braun 7 cm one-dimensional wire detector. Peak positions were calibrated using sodelite and silicon standards.

3. Results and discussion

3.1. Optical studies

In Fig. 1a–d we show low magnification images of the two-dimensional distribution of transmitted intensity in the blend samples during isothermal crystallization at 225°C under the condition that the sample is illuminated with purely left circularly polarized light

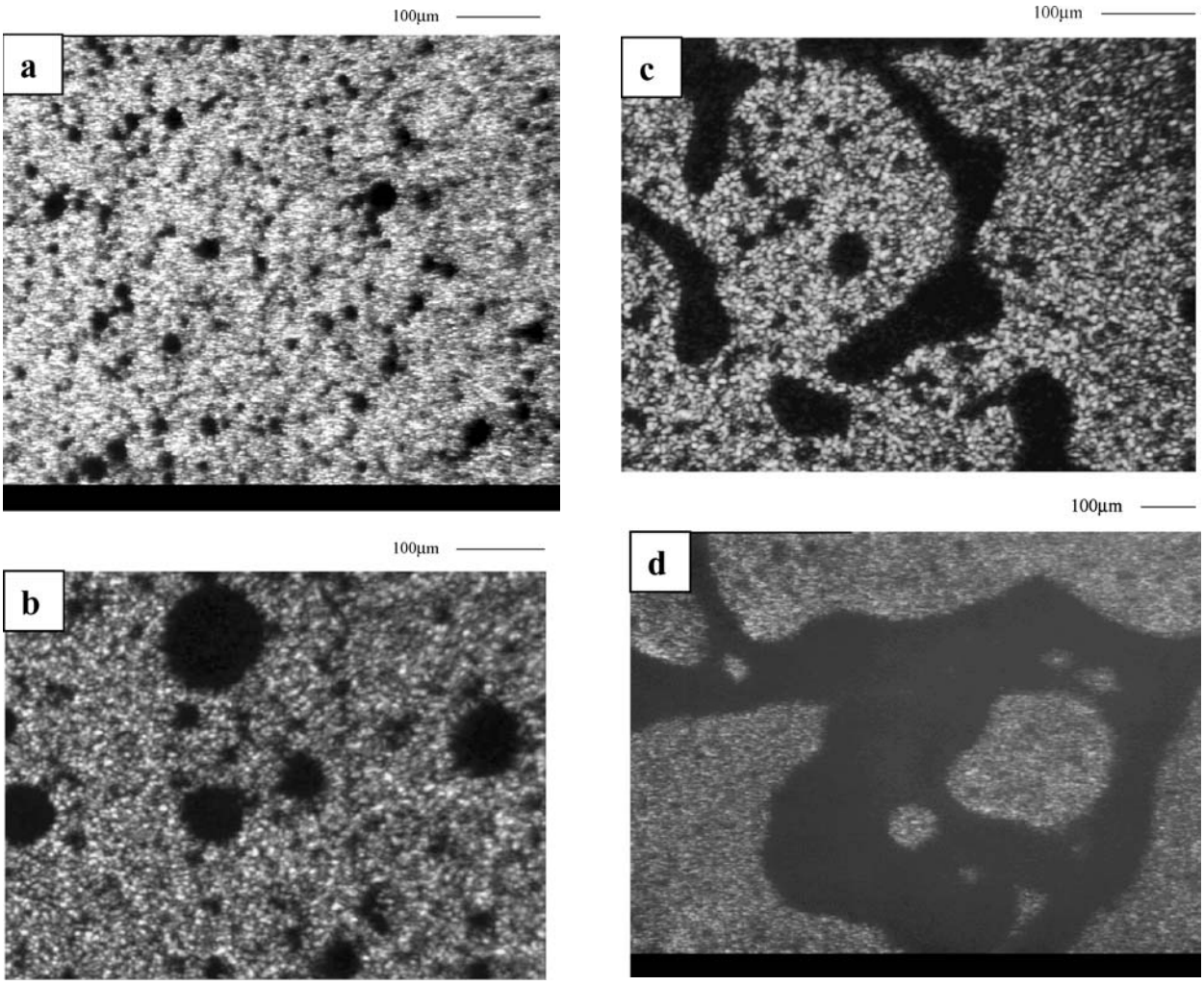

Figure 1 Transmitted intensity with full extinction of left circularly polarized light of PET/Vectra blends (a) 90/10; (b) 80/20; (c) 70/30; (d) 60/40. Intensity is measured at 225°C at the time when transmitted intensity is a maximum, during formation of the primary population of crystals. This time varies with blend composition, due to the differences in crystallization kinetics among the blends, and is within 3–6 minutes of temperature equilibration at 225°C.

using equipment described previously [41]. The incident radiation is incoherent but is monochromated at $\lambda = 55.3$ nm. The images are taken under polarization conditions with full extinction of left circularly polarized light. The time dependent changes of the transmitted intensity are followed, and correlated with the thermal and scattering methods of study considered in the next sections.

In Fig. 1, crystallized samples of PET/Vectra blends occur along with voids, which are seen as dark regions empty of matter. Around the voided regions, the development of spherulitic PET structures occurs during crystallization at 225°C. This is seen as the bright mottled regions representing PET spherulites that are too small to be individually resolved at the magnification used in the optical study. Higher magnification images (not shown) confirm that the spherulites are densely nucleated and hence quite small in all blends.

Transmitted intensity was quantitatively measured under polarization conditions of full extinction of left circular light. Fig. 2 shows the transmitted intensity for PET/Vectra blend 80/20 as a function of time during thermal treatment. The main features presented in Fig. 2 are the same for all blends examined, and 80/20 is shown as a representative example. The treatment conditions involve cooling from the melt, isothermal crystallization at 225°C, cooling to 215°C, and immediate reheating to melt the sample. At the beginning of the treatment at 290°C when the sample is melted, the only birefringent material is the Vectra component, which is in its nematic phase at this temperature. This intensity distribution does not change during the time when the sample temperature is decreasing at a rate of 5°C/min to 225°C. During the isothermal period there is induction time for PET crystal growth, the end of which is signified by Point 1. After a period of induction, the optical intensity begins to rise sharply as crystals of PET form. Eventually the PET spherulites start to impinge on each other and their rate of growth slows down. The growth of secondary PET crystals causes some depolarization, and the optical intensity decreases beginning at Point 2. Slow and steady decrease in intensity occurs until Point 3, at the end of the isothermal period. Then the temperature is decreased to 215°C, and intensity shows a small dip. Heating to 290°C begins immediately thereafter, and intensity starts to increase again. Points 4 and 5 correspond to PET melting transitions.

After all PET crystals melt, intensity drops sharply at Point 5 to the value indicated at Point 6 where now only the nematic Vectra component is birefringent. At 290°C where PET is completely melted, bright inhomogeneities remain in the optical images. This high intensity is due to the nematic ordering of the Vectra component of the blend since the PET melt is isotropic, and hence always appears black. Since the intensity is not homogenously distributed, we can conclude that nematic liquid crystalline Vectra is phase separated and forms birefringent domains within the PET melt.

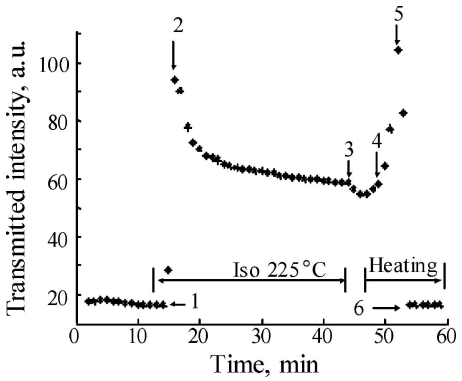

Figure 2 Transmitted intensity with full extinction of left circular light vs. time for PET/Vectra blend 80/20 in relative units integrated over an image area of 50 by 50 pixels. Sample was cooled from 290°C (first 11 min), crystallized isothermally at 225°C (for 12–44 min), cooled to 215°C (min 45–47), and then re-heated (min 48–60). Heating and cooling occurred at 5°C/min. Point 1 marks the end of the period during which only Vectra contributes to image intensity, and the start of crystal nucleation. Point 2 marks the maximum transmitted intensity and formation of primary crystals. Point 3 marks the end of the isothermal period. Point 4 marks the start of melting of the initial crystal population. Point 5 marks the start of melting of the reorganized crystal population. Point 6 marks the beginning of the period where only Vectra contributes.

3.2. Thermal analysis

DSC blend-normalized heat flow is shown in Fig. 3a and b for isothermal crystallization and subsequent melting, respectively, of PET/Vectra blends. Blend-normalized heat flow means the total heat flow measured for the

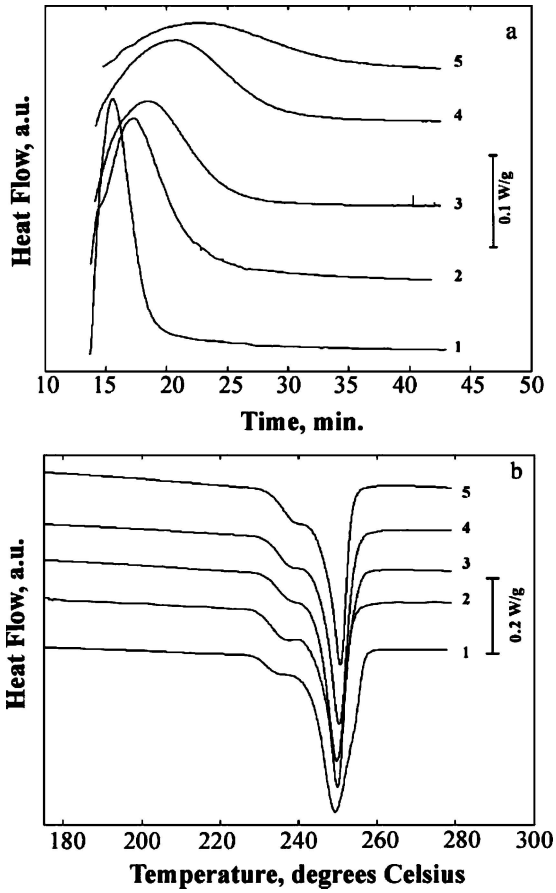

Figure 3 Normalized heat flow versus time for PET/Vectra blends 100/0 (curve 1), 90/10 (curve 2), 80/20 (curve 3), 70/30 (curve 4), 60/40 (curve 5) for: (a) isothermal crystallization at 225°C; (b) re-heating at 5°C/min. Heat flow has been normalized for blend composition. Curves are displaced vertically for clarity, and endotherms are indicated by downward deflections.

blend is divided by the weight fraction of the crystallizable PET component. Fig. 3a shows exothermic heat flow vs. time during isothermal crystallization at 225°C, and illustrates the kinetic dependence on the blend composition. The increase of Vectra content clearly slows the crystallization processes of PET causing the longest time to maximum heat flow in 60/40 blends. Although the crystallization process is affected by composition, the glass transition temperature ($T_g = 72.5 \pm 0.5$°C) for PET homopolymer and all four blends) is not. Using DSC, the glass transition temperature, after crystallization, was measured from the inflection point of the heat capacity step and results are included in Table I. The glass transition temperature is independent of the PET/Vectra content in the blend, because these two components are immiscible and remain phase separated before and after crystallization.

During isothermal crystallization, the maximum transmitted intensity (Fig. 2) occurs at the corresponding point where the shape of the heat flow curve during isothermal period changes to concave down (Fig. 3a). Initially, PET spherulites grow freely in a melt mixed with nematic liquid crystalline Vectra. Eventually, crystallization slows as the spherulites impinge upon their neighbors. The DSC exothermic heat flow begins to decrease, and the transmitted optical intensity also decreases. Crystallization continues at a slower pace, as smaller, later-formed spherulites still grow. At this point, the secondary population of less perfect crystals starts to form in the constrained environment of the amorphous phase, coexisting with the already formed primary crystals.

The subsequent melting after isothermal crystallization at 225°C is shown in Fig. 3b. All blends show dual melting peaks, which include a shoulder on the low temperature side of a sharp endotherm. The shoulder appears just above the crystallization temperature of 225°C. No endothermic heat flow occurs below 225°C, indicating that there is no additional crystallization occurring when the samples are cooled to room temperature. No samples showed the triple melting peaks that have been reported by other researchers for PET [22] or PET copolyesters [42]. The DSC melting endotherm starts immediately at 230°C just above the temperature of the thermal treatment and corresponds to Point 4 in Fig. 2. When the sample is reheated through the location of the lower endotherm (shoulder), the removal of the less perfect crystals has the effect of increasing the transmitted polarized intensity. The increase of the intensity continues throughout the lower endotherm (shoulder) and up to the maximum in the major endotherm. In spite of differences in the isothermal crystallization kinetics, the crystallinity of the PET component of the samples is almost the same, as shown in Table I

Schick and coworkers, using high heating rate nanocalorimetry [43, 44] have shown that PET crystals reorganize extremely rapidly. The uppermost endotherm disappeared when the PET was heated at rates on the order of 1000 K/s, leading these authors to conclude that: (1) PET reorganizes in about 40 ms (in the interval from 150 to 200°C) for PET crystallized at 130°C; and, (2) the uppermost endotherm is due to melting of reorganized crystals, and not to crystals initially formed at the isothermal crystallization stage. It is therefore likely that a similar effect occurs in PET/Vectra blends, so that the lower endotherm (showing as a shoulder in Fig. 3b) marks the location of melting of the preformed crystals, while the upper endotherm refers only to reorganized crystals.

The melting of all of the crystals leads to disappearance of most (but not all) of the transmitted polarized intensity. The large decrease of intensity in Fig. 2 from Point 5 to Point 6 during the final heating, corresponds to thermal transitions occurring at 250°C (Point 5) at the temperature of the melting endotherm in the DSC scan of the same sample shown in Fig. 3b. Residual transmitted polarized intensity is caused by the Vectra nematic liquid crystal component in the blends.

A limited study was done on non-isothermal melt-crystallization of 90/10 and 60/40 blends, and the data are not shown in the interests of brevity. Table II lists the thermal and structural parameters determined after non-isothermal cooling of these two compositions. Non-isothermal crystallization kinetics shows that 90/10 crystallizes at slightly higher temperature than 60/40 blends when the blends are cooled at 5°C/min. The mass fraction crystallinity, $f_{c,m}$ is a little larger in 60/40 blend ($f_{c,m} = 0.29$) compared to the 90/10 blend ($f_{c,m} = 0.27$).

3.3. WAXS analysis

WAXS intensity at the end of the isothermal period at 225°C is shown in Fig. 4 for all blends. An arrow marks

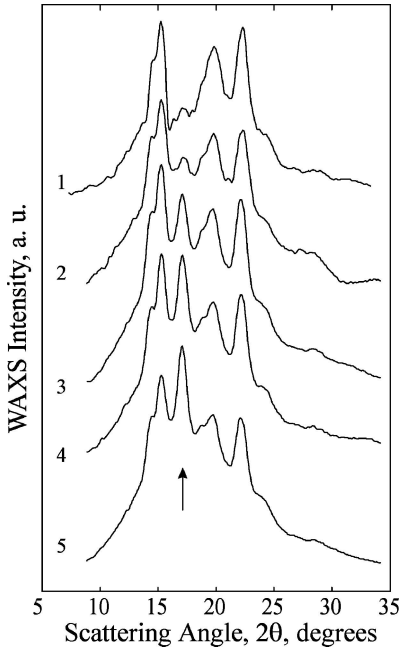

Figure 4 Relative WAXS intensity vs. scattering angle for $\lambda = 0.1366$ nm taken at the end of the isothermal period at 225°C for PET/Vectra blends 100/0 (curve 1), 90/10 (curve 2), 80/20 (curve 3), 70/30 (curve 4), 60/40 (curve 5). Curves are shifted vertically for clarity. The arrow points to the position of the scattering peak due to Vectra component in the blend at $2\theta = 17.1°$ [7].

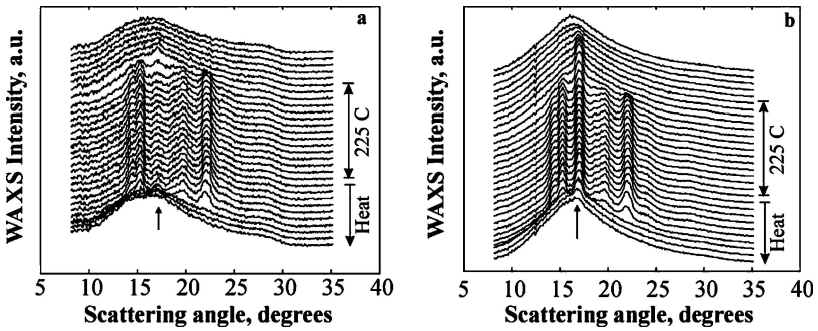

Figure 5 WAXS intensity vs. scattering angle for $\lambda = 0.1366$ nm for PET/VECTRA blends (a) 90/10, (b) 60/40. The time sequence starts at the top of the figure. Samples were cooled from 290°C at 5°C/min, held isothermally at 225°C for 30 min (as marked on the left of the plot), cooled to 215°C, and then heated at 5°C/min (as marked on the left of the plot). The arrow shows the position of the Vectra peak. Every curve represents one minute of data collection, and the curves are separated by a two-minute interval.

the location of the diffraction peak from Vectra nematic liquid crystal, which strengthens as the Vectra composition increases. X-ray results (at $\lambda = 0.1366$ nm) show that Vectra forms its nematic peak at $2\theta = 17.1^\circ$ with average distance between the aligned liquid crystalline segments of the polymer of 0.461 nm [7]. We also see the characteristic peaks of the PET triclinic structure, with Miller indices and d-spacings: (100) 0.349 nm, (−110) 0.397 nm, (010) 0.509 nm, and (0–10) 0.546 nm [45, 46].

The real-time development of the WAXS scattering peaks during thermal treatment is shown in Fig. 5a and b for blends 90/10 and 60/40, respectively. The sequence of scans runs from top to bottom in the figure, beginning with cooling from the melt, isothermal crystallization at 225°C, decrease to 215°C and reheating to 290°C. An arrow marks the location of the Vectra nematic WAXS reflection. The first and last scans, at the top and bottom of the figure, respectively, illustrate the difference Vectra content makes in the WAXS scan of molten blend. In the 90/10 blend (Fig. 5a), the amorphous melt halo is broad and only a small asymmetry due to Vectra's nematic liquid crystalline peak can be seen. Increased Vectra content, in the 60/40 blend (Fig. 5b), affects the shape of the WAXS peak in the scan of the molten blend, causing the amorphous halo to be strongly peaked at the location of the Vectra nematic liquid crystalline reflection. The intensity of the Vectra nematic phase scattering peak strengthens during cooling from 290°C from the isotropic melt, remains constant during the isothermal crystallization of PET, and weakens, again at higher temperature, during the reheating scan.

Fig. 6 shows the "crystallinity index" obtained from WAXS for blend 90/10. At the end of the crystallization, the amorphous melt curve (taken just before the start of crystallization) was scaled underneath the WAXS scan of the semicrystalline blend sample, using scaling points taken at two-theta values where there was no contribution from the crystalline peaks or the Vectra component. The scaled amorphous halo (including the contribution from the Vectra component) was subtracted from the total intensity. The ratio of the remaining crystal peak intensity to the total intensity is the "crystallinity index." A sharp increase of crystallinity is seen at the beginning of the isothermal period, and continued increase during that period occurs with additional crystallization of the amorphous phase. Upon heating, the WAXS crystallinity index decreases dramatically, and eventually reaches zero when the temperature increases above the main melting endotherm seen in DSC scans.

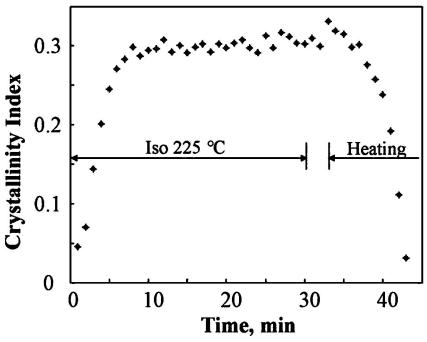

Figure 6 WAXS crystallinity index vs. time for PET/Vectra 90/10 blend during isothermal crystallization at 225°C, followed by cooling to 215°C and reheating at 5°C/min to 290°C.

3.4. SAXS analysis

In Fig. 7, we show the SAXS data for PET homopolymer at the end of isothermal crystallization at 225°C. The final Lorentz-corrected intensity and the correlation function, $\gamma(r)$, determined from Equation 7, are shown in Fig. 7a and b, respectively. The parameters $L^{\max}$ and d_1 are marked on the figure. The fraction of phase 1, ϕ_1, is found from $|A|/(|A| + Q)$ [38]. The correlation functions of the blends were similar to that of the homopolymer and will not be shown in the interests of brevity.

From Babinet's Principle, we cannot determine from SAXS alone, which of the two coherence lengths, d_1 or d_2 ($d_2 = L_{\max} - d_1$) represents the crystalline phase. Indeed this assignment had been the subject of much debate, with some groups [18, 23, 47–51] using the shorter length, d_1 and other groups [19, 21, 22, 52, 53] using the longer length, d_2, as the crystalline thickness. Recently, Jonas's group [23] correlated SAXS measurements with results of transmission electron microscopy to show that the shorter of the two correlation lengths, d_1, should be associated with the crystalline phase in the case of PET of crystalline fraction less

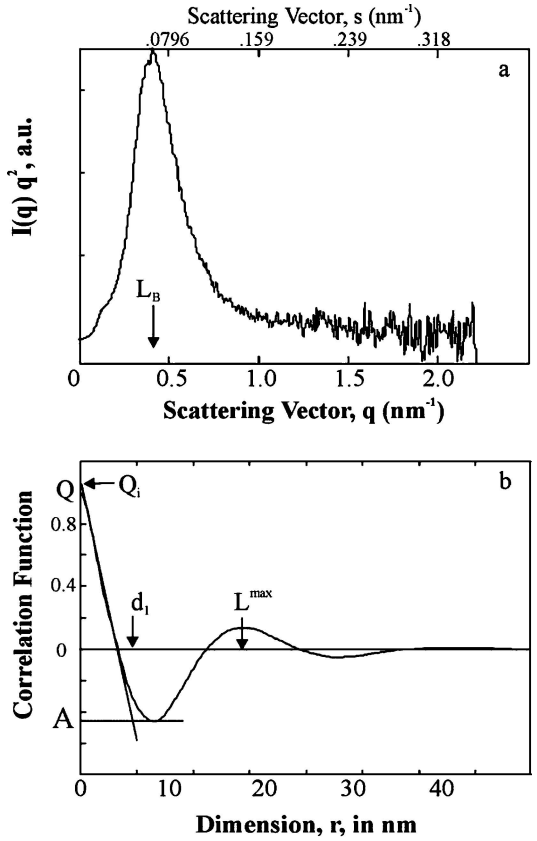

Figure 7 PET/Vectra 100/0 after 30 min of isothermal crystallization at 225°C. (a)Lorentz-corrected intensity, showing the location of the Bragg peak; (b) Normalized one dimensional electron density correlation function showing the location of d_1, the phase 1 thickness, L^{max}, the first maximum beyond $r = 0$, and the self-correlation triangle defined by intercepts A and Q_i. The ideal structure intercept, Q_i, is higher than the experimentally measured intercept, Q. $\lambda = 0.1366$ nm.

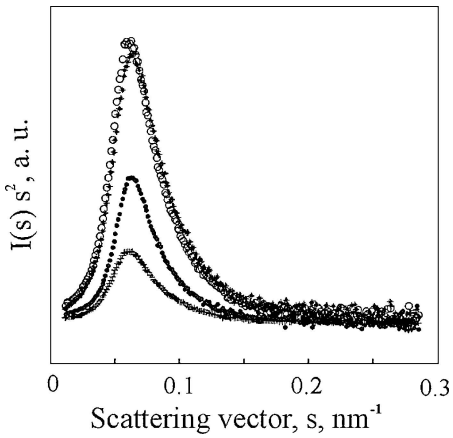

Figure 8 Lorentz corrected intensity, $I(s)s^2$, vs. scattering vector, s, for PET/Vectra blends after 30 min. of isothermal crystallization at 225°C, as a function of the blend composition. 90/10(*), 80/20°, 70/30 (·), 60/40 (+). $\lambda = 0.16$ nm.

than 0.50. Since in our PET/Vectra blends, we always observe crystalline fractions less than 0.45 (regardless of isothermal or non-isothermal crystallization conditions) we will assign the shorter of the two correlation lengths to the crystalline phase. This choice is also verified to be the proper one, based on consideration of the time dependence of the structural parameters, which will be presented later in Fig. 9.

Fig. 8 shows the final Lorentz corrected intensities for different compositions of PET/Vectra blends at the end of the isothermal crystallization period at 225°C. The peak position of the maximum does not vary much with composition, indicating that the average long period, L_B, is similar among the blends. The integrated scattering intensity, which relates to the scattering invariant, decreases strongly as the Vectra composition increases. Values of long period, d_1, and ϕ_1 derived from the correlation function for the intensities in Fig. 8, are listed in Table I.

The time development of the structural parameters from correlation function analysis is shown in Fig. 9a–d. The times shown in the figure start at the beginning of the isothermal period at 225°C, and continue through the subsequent reheating from 215 to 290°C. For clarity, the isothermal and heating portions are marked on two of the plots (a and d). The small gap between the arrows marks the brief cooling to 215°C. The figure shows the scattering invariant, Q_i (Fig. 9a), Bragg long period (Fig. 9b), lamellar thickness (Fig. 9c) and the linear stack crystallinity (Fig. 9d). The long period data and lamellar thickness are shown vertically shifted for clarity. Scattering invariant changes confirm that blends with higher Vectra content are slower to crystallize, indicated in Fig. 9a by the slope of the invariant with time at the beginning of the isothermal period. This correlates well with the DSC results shown in Fig. 3a. During the subsequent reheating, the scattering intensity decreases toward zero in the molten state.

From DSC results, the blends have about the same degree of crystallinity at the end of the isothermal period. Polarizing optical microscopy results also show that the samples are completely filled with crystalline entities (although individual spherulites are too small to be seen at optical magnifications). In spite of having similar degrees of crystallinity, from Fig. 5a we see that the scattering invariant systematically decreases as Vectra composition increases, during crystallization. This suggests that the scattering contrast factor in Equation 4 varies among the blends, causing the differences in scattering invariant. The scattering contrast, $\Delta\rho$, represents the electron density difference between the crystalline PET lamellae and the amorphous phase in between lamellae. As Vectra composition increases, the electron density difference between the PET lamellar crystals and the intervening amorphous phase decreases. This is a result of entrapment of nematic Vectra molecules within the amorphous phase. Vectra nematic liquid crystal has greater density (ρ(Vectra) = 1.40 g/cc [54]) than the amorphous PET phase (ρ_a(PET) = 1.335 g/cc [32]). As Vectra composition increases, more high-density Vectra is trapped in the amorphous regions reducing the electron density difference between the PET lamellae and the amorphous interlayer.

Variation of the long period, L^{max}, with time is shown in Fig. 9b, where curves have been separated vertically for clarity. The vertical dashed line is located at 30min, and the value of the long period at the 30 min mark can be obtained from Table I . During the isothermal period, a steady decrease in the long period is observed. Then, with the beginning of the heating period, L^{max} increases as a result of melting of the less perfect lamella first,

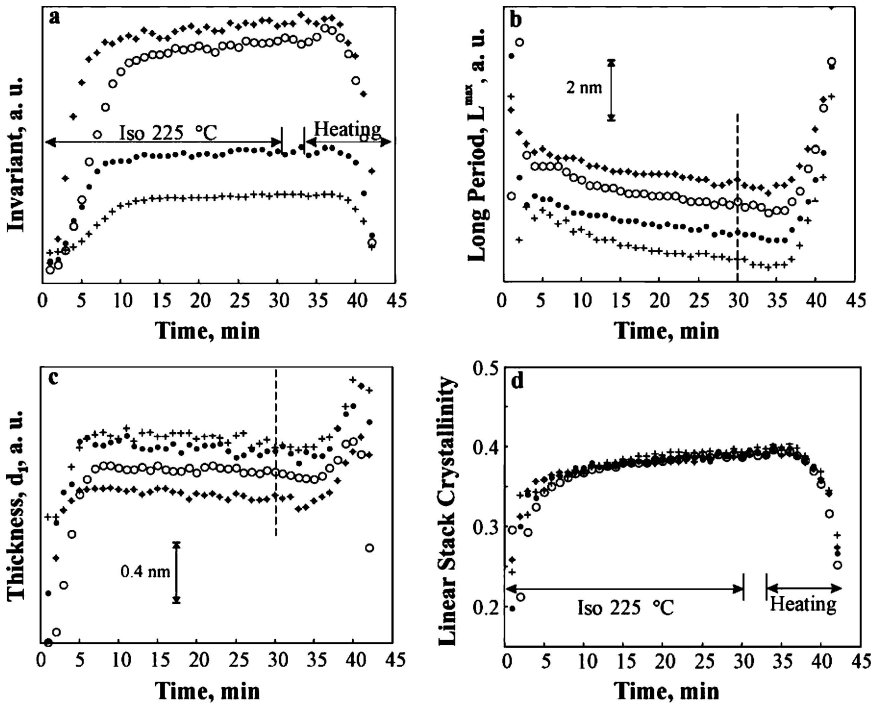

Figure 9 SAXS structural parameters from the correlation function vs. time for PET/Vectra blends 90/10(*), 80/20 (°), 70/30 (·), 60/40 (+). Blends were cooled from 290°C at 5°C/min, held isothermally at 225°C for 30 min, then cooled to 215°C before heating to 290°C at 5°C/min. The initial cooling from the melt is not shown. (a) Scattering invariant; (b) Long period, $L^{\max}$; (c) Lamellar thickness, d_1; (d) Linear stack crystallinity. Numerical values of $L^{\max}$ and d_1 at the 30 min mark (vertical dashed line) may be read from Table I. The horizontal regions in (a) and (d), marked "Iso 225C" and "Heating", pertain to all parts of the figure.

which increases the average interlamellar distance. By the time the temperature has reached the peak position of the main melting endotherm (the sharp endotherm in Fig. 3b), the long period is increasing to infinity, which corresponds to complete melting of all of the crystalline lamella. The trends observed here are similar to ones observed in our previous study of melt crystallization of PEEK/PEI blends [49].

Lamellar thickness variation is shown in Fig. 9c where curves have been separated vertically for clarity. The vertical dashed line is located at 30 min, and the value of d_1 at the 30 min mark can be obtained from Table I. For all blends, the lamellar thickness, d_1, is seen to increase in Fig. 9c at the beginning of the isothermal period. But after the maximum thickness is reached, continued crystallization in the constrained amorphous regions causes the average thickness to decrease slightly as crystallization proceeds. Upon heating, the originally crystallized lamellae melt first, forming the low temperature endothermic shoulder in Fig. 3b. As a result of reorganization and lamellar thickening, the average lamellar thickness increases. At the temperature of the main endotherm, the most perfect, reorganized, lamellae start to melt, and this causes a rollover of the trend of increase of the average lamellar thickness. Now, d_1 starts to decrease, eventually reaching the limiting value of zero (not shown in the figure), once all crystals are melted.

The parameters derived from the correlation function show that the shorter correlation length, d_1, can be correctly associated with the processes characteristic for the crystalline phase. As in our previous studies of poly(ether ether ketone)/poly(ether imide), PEEK/PEI, blends [49], the behavior of the shorter length has been shown to be typical of a crystalline, rather than an amorphous fraction of the sample, by following the time-dependent behavior of the lamellar thickness through melting. The lamellar thickness, d_1, decreases at the last stages of melting (Fig. 9c), while the thickness of the amorphous phase ($d_2 = L^{\max} - d_1$) will continue to increase, due to the melting of the less perfect lamellae leaving larger space between the still existing ones.

The crystalline fraction, $\phi_1 = d_1/L^{\max}$ in Fig. 9d sharply increases at the beginning of the isothermal period, and continues to increase gradually, due to additional crystallization, and insertion of less perfect lamellae. Upon heating, the ϕ_1 is seen to sharply decrease, to the limiting value of zero when temperature increases above the main melting endotherm, when all of the crystals are melted. The main trends in crystallinity index from WAXS (Fig. 6) are similar to the change in SAXS scattering invariant (Fig. 9a) and linear fraction of phase one (Fig. 9d).

For comparison with the isothermal study, Fig. 10a and b shows the time development during cooling of the long period and lamellar thickness, respectively, for PET/Vectra blends 90/10 (stars) and 60/40 (circles) crystallized non-isothermally. Both $L^{\max}$ and d_1 are smaller for the 60/40 blend, than for the 90/10 blend, over the entire temperature range. During non-isothermal crystallization, the Vectra component slows the initiation of the processes of crystallization, and the effect is most pronounced in blends with greatest Vectra content. The same effect was seen in the isothermal crystallization study (Fig. 3a). Here, by slowing the nucleation for 60/40 blend, this sample develops its crystals at slightly lower temperature, which results in the formation of less perfect lamella with smaller

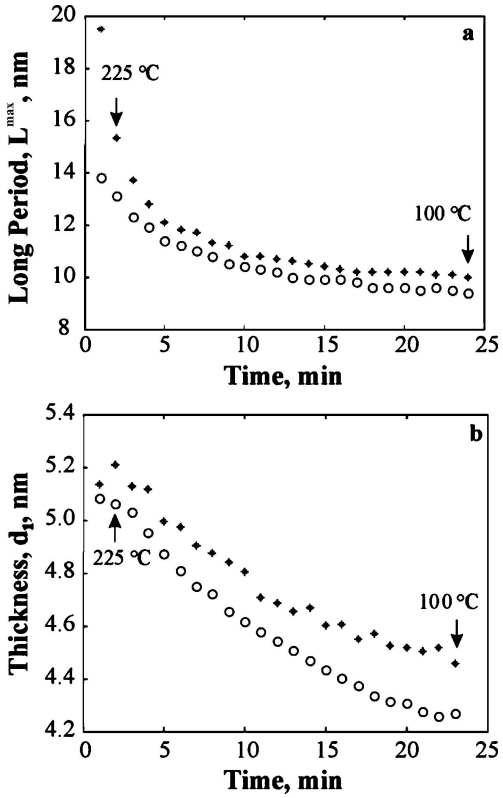

Figure 10 SAXS parameters during non-isothermal cooling of PET/VECTRA blends 90/10 (*) and 60/40(o) at 5°C/min. Each minute on the x-axis represents 5°C temperature interval. (a) Long period; (b) Lamellar thickness.

lamellar thickness. The influence of Vectra is seen in both isothermal and non-isothermal crystallization kinetics and resultant structural parameters.

When the crystalline fraction is calculated from $d_1/L^{\max}$, we find that both 90/10 and 60/40 blends have the same fraction of crystal PET in the lamellar stacks, i.e., $\chi_c = 0.44$. However, the crystalline phase fraction is much larger than the volume fraction crystallinity determined from DSC, which shows that a larger fraction of the PET component is located in amorphous regions outside the crystalline stacks. Vectra is also in the amorphous regions, which does not interfere with the conclusion that more of the amorphous phase of PET is also outside the crystalline stacks when the blends are crystallized non-isothermally.

In our previous study of miscible blends of PEEK/PEI [49], a similar effect on crystallization kinetics was seen whereby the non-crystallizable component leads to slowing of the nucleation processes for formation of crystals in the crystallizable component. The delay of nucleation to lower temperatures results in a decrease in perfection of the crystalline structures. During *isothermal* crystallization of PET/Vectra blends, an increase in induction time for crystal growth as Vectra content increases allows additional time for defect expulsion from the crystals and results in more perfect crystals forming isothermally in the high-Vectra content blends. This same process, delay of nucleation, in *non-isothermal* crystallization now leads to less perfect crystals. At lower temperatures crystallization is occurring faster and does not allow the same degree of crystal perfection. The DSC results show that the non-isothermal crystallization produces a decrease in the total crystallinity compared to the isothermal case, but there is an increase in the linear stack crystallinity. This means that more amorphous PET is stranded outside the crystalline stacks in the non-isothermal case.

Finally, the method of Ruland and Stribeck [25–28] was used to determine the interface distribution function, IDF, and typical results are shown in Fig. 11a and b for PET/Vectra blends 100/0 and 60/40, respectively. The symbols represent calculation of the IDF from data using Equation 5. Gaussian fits from Equation 6, assuming a stacking model with infinite stacks (ISSM), resulted in the solid curve, whose first six terms are shown by the dashed-line Gaussians. The fits are similar to those determined by others for PET homopolymer [21] and PET co-polyesters [42]. Starting from lowest values of r, the first two positive-going Gaussians (peak positions, d_1 and d_2), the first negative-going Gaussian (peak position, L) and their variances are listed in Table I. In the ISSM, restrictions are imposed on lengths and variances, such that lengths d_1 and d_2 are independent, while L and all higher order interface lengths are dependent on them, and variances σ_1 and σ_2 are independent, and all others are dependent upon them [25].

The IDF gives similar trends when the PET homopolymer is compared to its blends with Vectra. The long period, L, is shorter in PET/Vectra 100/0 (L = 12.0 nm), while the blends have longer L(L = 13.3–13.7 nm) that does not show systematic dependency upon composition. The same is generally true of the

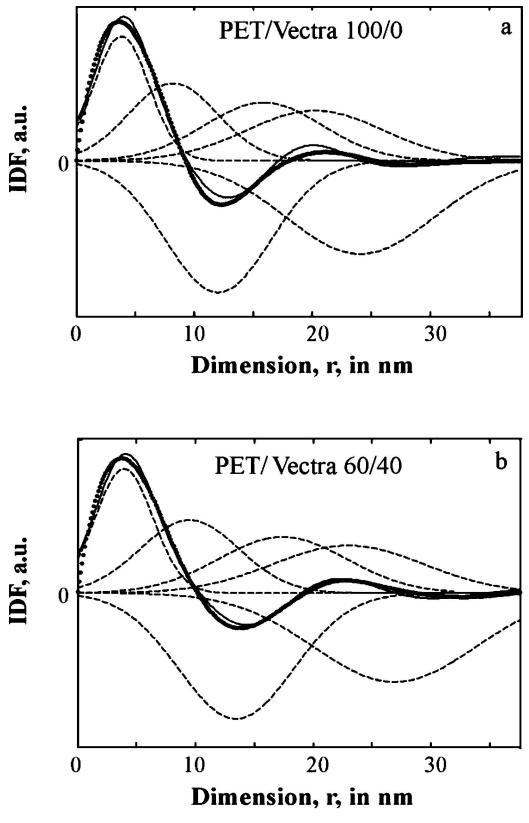

Figure 11 Interface distribution function, $g_1(r)$ at the end of isothermal crystallization at 225C, for PET/Vectra blends: (a) 100/0, (b) 60/40. Determined from: Equation 5—circles; best fit to Equation 6—solid line; first six Gaussians in the summation of Equation 6—dashed lines.

crystal thickness, d_1, the exception being the 60/40 blend, which has a value of d_1 close to that of homopolymer PET.

The values of long period and phase thickness derived from the IDF are deemed more accurate than those derived from the correlation function [19] or maximum in Is^2. Systematic variations are seen in the long period among the different methods. In comparing the long period obtained from the IDF to the long period from correlation function or Bragg's peak, the following trend is seen: $L(\mathrm{IDF}) < L^{\max} < L_{\mathrm{B}}$. This difference has been accounted for by Santa Cruz *et al*. [19]. Values of $L^{\max}$ and d_1 from the correlation function are shifted to larger values because of the breadth of the amorphous phase distribution as reflected in σ_2. From Table I, we observe that, in all sample studied, both the crystal phase variance, σ_1, and amorphous phase variance, σ_2, are broad, but σ_2 is nearly twice σ_1. Thus, the explanation provided for the trend of long period derived by different methods in homopolymer PET [19] may apply also to blends of PET with Vectra.

4. Conclusions

We investigated in binary polymer blends the effects of non-crystallizable immiscible liquid crystal polymer component on the crystallization, and degree of perfection of the crystals, of the semicrystalline polymer component. PET is a semicrystalline polymer forming lamellar structure, and spherulitic morphology. Vectra is a nematic liquid crystalline polymer, which cannot form lamellae, and forms phase separated domains within the PET melt.

Vectra slows the process of crystallization of PET, thus influencing the structure of the semicrystalline PET. With increasing Vectra content, PET isothermal crystallization kinetics are slowed. The time to the maximum heat flow increases as Vectra content increases. Therefore, as Vectra content increases: (a) Isothermal crystallization at high temperature makes the PET lamellae more perfect because of the longer time allowed for crystallization; and, (b) Non-isothermal crystallization makes the PET lamellae less perfect, because of delayed nucleation and the lower temperature of crystal formation.

We addressed the controversy about the induction role of Vectra on PET crystallization, and now we can conclude that the role that Vectra plays is not confined to a single aspect, but it depends on the conditions of crystallization and could be two-fold: first, to slow the processes of crystallization, and second, to make crystals more perfect when they are grown isothermally and less perfect when they are grown non-isothermally.

Also, the controversy of whether the amorphous phase is situated in the interlamellar regions or in amorphous pockets, can be answered by the fact that the DSC crystallinity is slightly smaller than the lamellar stack crystallinity measured by SAXS in the isothermally crystallized blends. A larger difference is observed when the blends are non-isothermally crystallized. This allows the conclusion that some amorphous PET phase must be outside the lamellar regions in separate areas, but the amount is small in the case of isothermally crystallized blends. The trends in $L^{\max}$ and d_1 with time during crystallization and reheating furthermore suggest that the thickness $d_1 (d_1 < d_2)$ should be adopted as the crystal lamellar thickness in agreement with the results of Haubruge *et al*. [23].

Acknowledgements

Research was supported by the National Aeronautics and Space Administration, Grant NAG-1480, and by the National Science Foundation, Polymers Program of the Division of Materials Research, Grant DMR 0100646. The authors thank Mr. Brian Feinberg for assistance with ellipsometry and Mr. Nathan Gilfoy for assistance in the thermal data collection. A portion of the work was conducted at the Brookhaven National Synchrotron Light Source, beamlines X12B and X27C.

References

1. A. DONALD and A. WINDLE, in "Liquid Crystalline Polymers" (Cambridge University Press, Cambridge, GB, 1992).
2. M. NAFFAKH, M. GOMEZ, G. ELLIS and C. MARCO, *Polym. Intern.* **52**(12) (2003) 1876.
3. F. TORRE, M. CORTAZAR, M.GOMEZ, G.ELLLIS and C. MARCO, *Polym.* **44**(18) (2003) 5209.
4. *Idem., J. Polym. Sci.Part B, Polym. Phys*. **42**(10) (2004) 1949.
5. A. MARINELLI and R. BRETAS, *J. Appl. Polym. Sci*. **87**(6) (2003) 916.
6. A. KALKAR and V. KUNTE, *Molec. Cryst. Liq. Cryst.* **383** (2002) 1.
7. I. CAMPOY, M. GOMEZ and C. MARCO, *Polym.* **39**(25) (1998) 6279.
8. B. LIANG, L. PAN and X. HE, *J. Appl. Polym. Sci.* **66**(2) (1997) 217.
9. H. CHIN and F. CHANG, *Polym.* **38**(12) (1997) 2947.
10. W. KIM and M. DENN, *J. Rheol*. **36**(8) (1992) 1477.
11. P. TANG, J. REIMER and M. DENN, *Macromol.* **26**(16) (1993) 4269.
12. P. MAGAGNINI, M. TONTI, M. MASSETI, M. PACI, L. MINKOVA, T. MITEVA, *Polym. Eng. Sci*. **38** (1998) 1572.
13. A. SMITH, C. BAI, H. ADE, R. SPONTAK, C. BALIK and C. KOCH, *Macromol. Rapid Commun*. **19** (1998) 557.
14. G. CHANG-CHIEN and M. DENN, *Polym. Adv. Techn.* **7** (1996)168.
15. M. SILVERSTEIN, A. HILTNER and E. BAER, *J. Appl. Polym. Sci*. **43**(1) (1991) 157.
16. W. PERKINS, A. MARCELLI and H. FRERKING, *ibid.* **43**(2) (1991) 329.
17. C. ZHOU, J. MA, B. LIANG, R. JIANG and X. REN, *Acta Polymerica Sinica* **5** (2001) 565.
18. A. JONAS, T. RUSSELL and D. YOON, *Coll. Polym. Sci.* **272** (1994) 1344.
19. C. SANTA CRUZ, N. STRIBECK, H. G. ZACHMANN and F. BALTA CALLEJA, *Macromol.* **24** (1991) 5980.
20. R. GERKE, C. RIEKEL and H. G. ZACHMANN, *Polym.* **30**(9) (1989) 1582.
21. C. ALVAREZ, I. SICS, A. NOGALES, Z. DENCHEV, S. S. FUNARI and T. A. EZQUERRA, *ibid.* **45** (2004) 3953.
22. C. A. AVILA-ORTA, F. J. MEDELLIN-RODRIQUEZ, Z. WANG, D. NAVARRO-RODRIQUEZ, B. S. HSIAO and F. YEH, *Polym*. **44**(5) (2003) 1527.
23. H. HAUBRUGE, A. JONAS and R. LEGRAS, *Macromol.* **37**(1) (2004) 126.
24. Z. XIA, H-J. SUE, Z. WANG, C. A. AVILA-ORTA and B. S. HSIAO, *J. Macromol. Sci.-Phys*. **40**(5) (2001) 625.
25. N. STRIBECK and W. RULAND, *J. Appl. Cryst*. **11** (1978) 535.
26. N. STRIBECK, *Colloid Polym. Sci*. **271** (1993) 1007.
27. *Idem., J. Phys. IV* **3**(C8) (1993) 507.
28. *Idem., Colloid Polym. Sci*. **280** (2002) 254.
29. F. J. MEDELLIN-RODRIQUEZ and C. A. AVILA-ORTA, *Avances en Ingenieria Quimica* **6**(2) (1996) 156.

30. J. KUGLER, J. W. GILMER, D. WISWE, H. G. ZACHMANN, K. HAHN and E. W. FISCHER, *Macromolecules* **20** (1987) 1116.
31. G. TOVAR, P. J. CARREAU and H. P. SCHREIBER, *Colloids Surf. A: Physicochem. Engng. Aspects* **161**(1) (2000) 213.
32. J. BRAUNDRUP and E. IMMERGUT (eds.), in "Polymer Handbook" (John Willey & Sons, NY, 1980).
33. K. H. ILLERS, *Colloid Polym. Sci.* **258** (1980) 117.
34. W. RULAND, *ibid.* **255**(5) (1977) 29.
35. J. T. KOBERSTEIN, B. MORRA and R. S. STEIN, *J. Appl. Cryst.* **13** (1980) 34.
36. MATLAB^{TM} (The Mathworks, Natick, MA, 2000).
37. C. VONK and G. KORTLEVE, *Kolloid-Zeitschrift und Zeitschrift fur Polymere* **220**(1) (1967) 19.
38. G. STROBL and M. J. SCHNEIDER, *Polym. Sci.: Part B: Polym. Phys.* **18** (1980) 1343.
39. P. CEBE, in "Introduction to Scattering From Polymers" "Scattering From Polymers: Characterization by X-rays, Neutrons and Light," edited by P. Cebe, B. Hsiao and D. Lohse (American Chemical Society, Washington, DC, 2000).
40. O. GLATTER and O. KRATKY, in "Small Angle X-ray Scattering" (Academic Press, London, 1982).
41. G. GEORGIEV, D. BERNS and P. CEBE, *Amer. Chem. Soc., Proc. Div. Polym. Mater.: Sci. and Eng.* **84** (2001) 1012.
42. F. J. MEDELLIN-RODRIQUEZ, P. J. PHILLIPS, J. S. LIN and C. A. AVILA-ORTA, *J. Polym. Sci., Part B: Polym. Phys.* **36** (1998) 763.
43. A. M. MINAKOV, D. A. MORDVINTSEV and C. SCHICK, *Polym.* **45** (2004) 3755.
44. *Idem.*, *Faraday Discussions* **128** (2004) 261.
45. C. MCDOWELL, B. D. FREEMAN, G. W. MCNEELY, M. I. HAIDER and A. J. HILL, *J. Polym. Sci. Part B: Polym. Phys.* **36** (1998) 2981.
46. C. MCDOWELL, B. D. FREEMAN and G. W. MCNEELY, *Polym.* **40** (1999) 3487.
47. A. JONAS, T. RUSSELL and D. YOON, *Macromol.* **28** (1995) 8491.
48. C. FOUGNIES, P. DAMMON, D. VILLERS, M. DOSIERE and M. KOCH, *Macromol. 30* (1997) 1385.
49. G. GEORGIEV, P. CEBE and M. CAPEL, *J. Mater Sci.* **36**(6) (2001) 1349.
50. G. GEORGIEV, N. GILFOY, P. CEBE and M. CAPEL *Polym.* **45**(10) (2004) 3429.
51. N. BASKARAN, H. XU, B. S. INCE and P. CEBE, *J. Polym. Sci. Part B: Polym. Phys.* **42**(5) (2003) 777.
52. R. VERMA, H. MARAND and B. HSIAO, *Macromol.* **29** (1985) 7767.
53. R. VERMA and B. HSIAO, *Trends Polym. Sci.* **4** (1996) 312.
54. http://www.goodfellow.com/csp/active/static/A/ES31.HTML

Received 30 August
and accepted 8 November 2004